Quantum beat oscillations in the two-color-photoionization continuum of neon and their dependence on the intensity of the ionizing laser pulse

Henning Geiseler, Horst Rottke, Günter Steinmeyer, and Wolfgang Sandner
Max-Born-Institut für Nichtlineare Optik und Kurzzeitspektroskopie, Max-Born-Straße 2 A, D-12489 Berlin, Germany
(Received 22 July 2011; published 29 September 2011)

We investigate quantum beat oscillations in the photoionization continuum of Ne atoms that are photoionized by absorption of two photons via a group of excited bound states using ultrashort extreme ultraviolet and infrared laser pulses. The extreme ultraviolet pulse starts an excited-state wave packet that is photoionized by a high-intensity infrared pulse after a variable time delay. We analyze the continuum quantum beats from this two-step photoionization process and their dependence on the photoelectron kinetic energy. We find a pronounced dependence of the quantum beat amplitudes on the photoelectron kinetic energy. The dependence changes significantly with the applied infrared laser-pulse intensity. The experimental results are in good qualitative agreement with a model calculation that is adapted to the experimental situation. It accounts for the intensity dependence of the quantum beat structure through the coupling of the excited-state wave packet to other bound Ne states induced by the high-intensity infrared laser pulse.

DOI: 10.1103/PhysRevA.84.033424 PACS number(s): 42.50.Md, 42.50.Hz, 32.80.Fb, 32.80.Qk

I. INTRODUCTION

Quantum beats in the total photoionization yield are found when a time-dependent bound-state electron wave packet is photoionized using a laser pulse that is short compared to the time evolution of this wave packet. The beating of the photoionization yield reflects the energy differences between the involved bound states that make up this wave packet. These quantum beats have been used to trace, for example, a Rydberg electron on its orbit [1] and electron spin precession in coherently excited fine structure levels [2]. They are also detectable in differential photoelectron-kinetic-energy and angular distributions [3,4].

Here we describe and interpret quantum beat oscillations observed in the photoelectron-kinetic-energy distribution when an atomic system is photoionized by absorption of two laser photons via bound electronic states. The model system we used in this investigation is the neon atom. We find that the quantum beats map bound-state dynamics induced by a high-intensity ionizing laser pulse into the kinetic-energy distribution of the photoelectrons. This specifically means that the quantum beat structures sensitively depend on the intensity of the ionizing laser pulse, which simultaneously induces population transfer among bound states and ac Stark shifts of these states.

Quantum beats in the photoionization continuum at specific electron kinetic energies are found, provided that the same final state of the system consisting of the photoion and the photoelectron can be reached via several distinct quantum paths. In our case, this is accomplished by employing spectrally broad ultrashort laser pulses. A first pulse excites a group of bound states (i.e., starts a wave packet), which is then photoionized after a tunable delay by a second high-intensity pulse [see Fig. 1(a)]. The first pulse is weak and can be treated in a perturbative way. In case of sufficient spectral width it is possible to arrive at the same ionic state and photoelectron kinetic energy via several distinct quantum paths. This is equivalent to saying that the pulse width is short compared to the time scale of the wave-packet dynamics in the group of bound states excited by the first pulse. The specific situation is shown in the inset in Fig. 1(a). In the spectral overlap region of two quantum paths, beat oscillations are observed in the photoelectron-kinetic-energy distribution when scanning the ionizing laser pulse delay. In the simplest case, the amplitudes of the quantum beats are basically products of the Fourier amplitudes of the two laser pulses multiplied by corresponding transition dipole matrix elements; i.e., they are independent of atomic dynamics. In this case, atomic bound-state dynamics only enters via the beat frequencies that represent the energy differences between the unperturbed bound electronic states involved. This behavior changes significantly when the second ionizing laser pulse becomes strong, as is the case in our investigation. The pulse modifies the unperturbed bound-state dynamics when it is turned on after a delay with respect to the first exciting laser pulse. Depending on the intensity of the ionizing pulse, the quantum beat amplitudes in the photoelectron-kinetic-energy distribution change accordingly.

The paper is organized as follows. In the next section we present a theoretical model that is able to describe the spectral distribution of the quantum beat amplitudes and their dependence on the ionizing laser-pulse intensity. Our experimental setup is described in Sec. III. In Sec. IV the experimental results are presented and in Sec. V they are compared with specific model calculations that are based on the theoretical model introduced in Sec. II.

II. THEORETICAL MODEL

The resonant two-photon ionization of neon, which we are investigating, is schematically shown in the energy level diagram in Fig. 1(b). From the neon ground state ϕ_0 we first excite a coherent superposition of bound states ϕ_i ($i = 2, \ldots, n$) with an xuv laser pulse. Its spectral bandwidth covers several Ne absorption lines from the ground state. An ir pulse follows the xuv pulse after a variable delay δ [see Fig. 1(b)]. This pulse probes the group of excited states via one-photon photoionization. The broad spectral width of the ir pulse allows reaching each final continuum state via several

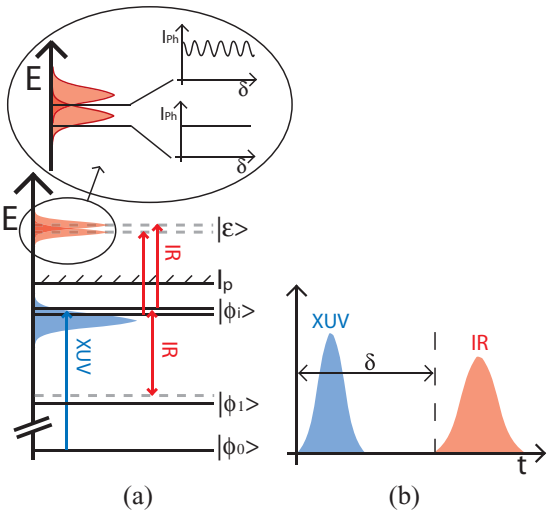

FIG. 1. (Color online) (a) Schematic view of the investigated photoionization mechanism. An xuv pulse excites the atomic system to a coherent superposition of states $|\phi_i\rangle$. A high-intensity ir pulse then couples the wave packet formed to a lower-lying state $|\phi_1\rangle$ while ionizing the system at the same time. As the inset shows, quantum beat oscillations may only occur in the photoelectron-kinetic-energy distribution in those energy regions that can be reached from several of the involved intermediate states. (b) Schematic view of the pulse sequence that is applied to the atomic system. The delay δ between the pulses is variable.

of the intermediate bound states. The corresponding different quantum paths to a specific continuum final state therefore give rise to interference phenomena in the ionization continuum [see the inset in Fig. 1(a)]. These interferences depend on the delay of the ir with respect to the xuv pulse. In addition to ionizing the group of states $\phi_2,\ldots,\phi_n$, the ir pulse couples these states nearly resonantly to a lower-lying bound state ϕ_1 [see Fig. 1(a)]. As described in the following, this bound-bound state coupling gives rise to a dependence of the interference phenomena in the photoelectron-kinetic-energy distribution on the ir pulse intensity.

In order to model this situation, we assume that the xuv excitation and similarly the ir ionization step of the intermediate bound states $\phi_2,\ldots,\phi_n$ may be described by lowest-order perturbation theory. The final continuum states are assumed to be unaffected by the ir radiation. However, we assume that the coupling of the bound states $\phi_2,\ldots,\phi_n$ to the lower-lying state ϕ_1 through the intense ir pulse has to be described in a nonperturbative way. The starting point for the theoretical analysis is the integral equation for the propagator $U(t,t_0)$ for a system described by the Hamiltonian $H = H_0 + V(t)$:

$$U(t,t_0) = U_0(t,t_0) - i\int_{t_0}^{t} dt'\; U(t,t')V(t')U_0(t',t_0)$$

with $U_0(t,t_0)$ being the propagator that corresponds to H_0 in the decomposition of the total Hamiltonian H given above (atomic units are assumed; see, for example, [5,6]). Using this equation, the exact transition amplitude $a_{(\lambda,\epsilon)}(T)$ from the atomic initial state ϕ_0 to a final continuum state $\phi_{(\lambda,\epsilon)}$ at the end of the xuv-ir pulse sequence can be expressed in the form

$$\begin{aligned} a_{(\lambda,\epsilon)}(T) = -i\int_0^T dt\,\langle\phi_{(\lambda,\epsilon)}|\tilde{U}_0(T,t)V(t)U_0(t,0)|\phi_0\rangle \\ -\int_0^T dt\int_t^T dt'\langle\phi_{(\lambda,\epsilon)}|U(T,t')\tilde{V}(t')\tilde{U}_0(t',t) \\ \times V(t)U_0(t,0)|\phi_0\rangle \end{aligned} \quad (1)$$

after iterating the above integral equation once. Here $U(t_2,t_1)$ is the exact propagator for the atomic system in the externally applied laser pulses; (λ,ϵ) characterizes the final continuum state of the unperturbed atomic Hamiltonian H_0 with energy ϵ and λ representing further discrete quantum numbers; and $\tilde{H}_0$ and $\tilde{V}$ correspond to a second decomposition of $H = \tilde{H}_0 + \tilde{V}$ with $\tilde{U}_0(t_2,t_1)$ the propagator corresponding to the Hamiltonian $\tilde{H}_0$.

Using the dipole approximation for the atom–light pulse interaction, the Hamiltonian for this system reads

$$H(t) = H_0 + \boldsymbol{F}_X(t)\boldsymbol{d} + \boldsymbol{F}_I(t)\boldsymbol{d},$$

with H_0 the Hamiltonian of the unperturbed atom, $\boldsymbol{d}$ the dipole operator, $\boldsymbol{F}_X(t)$ the time-dependent electric field of the xuv pulse, and $\boldsymbol{F}_I(t)$ that of the ir pulse. $V(t)$ in Eq. (1) is then assumed to be given by

$$V(t) = \boldsymbol{F}_X(t)\boldsymbol{d} + \boldsymbol{F}_I(t)\boldsymbol{d}.$$

$U_0(t_2,t_1)$ is the propagator of the unperturbed atomic system that is characterized by the Hamiltonian H_0.

The light intensities used in the experiment allow the following approximations to be made in the transition amplitude $a_{(\lambda,\epsilon)}(T)$. Given the specific choice of $\tilde{U}_0(T,t)$ below, the integral in the first line of Eq. (1) can be neglected. With this choice, the integral represents basically a one-photon transition from the ground state to the ionization continuum. Such a transition practically does not contribute to the transition amplitude in the energy range of interest. Furthermore, we assume that the continuum states are not modified by the laser pulses and that continuum-continuum transitions have a negligible probability. Accordingly, in the double integral of Eq. (1) we replace the exact propagator $U(T,t')$ by the propagator of the unperturbed atomic system, $U_0(T,t')$. In $V(t)$ only the xuv-pulse contribution gives rise to transitions from ϕ_0 to the bound excited states ϕ_i $(i = 2,\ldots,n)$. The expression for the transition amplitude to the continuum can thus be approximated by

$$\begin{aligned} a_{(\lambda,\epsilon)}(T) \approx -\sum_{i=2}^{n}\int_0^T dt\int_t^T dt'\; e^{i\epsilon(t'-T)-iE_0t}\langle\phi_{(\lambda,\epsilon)}|\tilde{V}(t') \\ \times\tilde{U}_0(t',t)|\phi_i\rangle[\boldsymbol{F}_X(t)\boldsymbol{d}_{i,0}]. \end{aligned} \quad (2)$$

Here the $\boldsymbol{d}_{i,0} = \langle\phi_i|\boldsymbol{d}|\phi_0\rangle$ represent the dipole matrix elements for the transition from the atomic ground state to the states ϕ_i $(i = 2,\ldots,n)$.

The interaction potential $\tilde{V}(t)$ and the propagator $\tilde{U}_0(t_2,t_1)$ that appear in the expressions for the transition amplitude in Eqs. (1) and (2) correspond to a second partitioning of the full Hamiltonian $H(t)$. This partitioning is adapted to describe the effect of the ir laser pulse on the excited atomic states. If P

represents the projector that projects on the space spanned by the unperturbed excited atomic states $\{\phi_i, i = 1, \ldots, n\}$ and $Q = \mathbf{I} - P$ (with $\mathbf{I}$ the identity operator) projecting on the corresponding orthogonal space, $H(t)$ may be written as

$$H(t) = PHP + PHQ + QHP + QHQ.$$

We now partition $H(t)$ into $H = \tilde{H}_0 + \tilde{V}$ with

$$\begin{aligned} \tilde{H}_0 &= PHP, \\ \tilde{V} &= PHQ + QHP + QHQ. \end{aligned} \tag{3}$$

$\tilde{U}_0(t_2,t_1)$ is the propagator that corresponds to the Hamiltonian $\tilde{H}_0$. Substituting this partitioning into Eq. (2), the transition amplitude to the continuum can be written as

$$\begin{aligned} a_{(\lambda,\epsilon)}(T) \approx -\sum_{i=2}^{n}\sum_{j=1}^{n}\int_0^T dt \int_t^T dt'\, e^{i\epsilon(t'-T)-iE_0t} \\ \times\langle\phi_{(\lambda,\epsilon)}|\tilde{V}(t')|\phi_j\rangle\langle\phi_j|\tilde{U}_0(t',t)|\phi_i\rangle[\boldsymbol{F}_X(t)\boldsymbol{d}_{i,0}]. \end{aligned} \tag{4}$$

With its definition in Eq. (3) the matrix element of $\tilde{V}(t)$ in Eq. (4) reduces to

$$\begin{aligned} \langle\phi_{(\lambda,\epsilon)}|\tilde{V}(t)|\phi_j\rangle &= \langle\phi_{(\lambda,\epsilon)}|QHP|\phi_j\rangle \\ &= \langle\phi_{(\lambda,\epsilon)}|[\boldsymbol{F}_X(t)\boldsymbol{d} + \boldsymbol{F}_I(t)\boldsymbol{d}]|\phi_j\rangle \\ &\approx \langle\phi_{(\lambda,\epsilon)}|\boldsymbol{F}_I(t)\boldsymbol{d}|\phi_j\rangle \\ &= \boldsymbol{F}_I(t)\boldsymbol{d}_{(\lambda,\epsilon),j}, \end{aligned} \tag{5}$$

with $\boldsymbol{d}_{(\lambda,\epsilon),j}$ the dipole matrix element for bound-free transitions. The approximation made here is based on the fact that continuum transitions induced by the xuv pulse starting from the bound excited atomic states are negligible.

With all approximations introduced, the transition matrix element to the continuum reads

$$\begin{aligned} a_{(\lambda,\epsilon)}(T) \approx -\sum_{i=2}^{n}\sum_{j=1}^{n}\int_0^T dt \int_t^T dt'\, e^{i\epsilon(t'-T)-iE_0t} \\ \times[\boldsymbol{F}_I(t')\boldsymbol{d}_{(\lambda,\epsilon),j}][\boldsymbol{F}_X(t)\boldsymbol{d}_{i,0}]\langle\phi_j|\tilde{U}_0(t',t)|\phi_i\rangle. \end{aligned} \tag{6}$$

The dynamics in the intermediate bound excited states is driven by the ir laser pulse alone. This means that

$$\tilde{H}_0 = PHP \approx P[H_0 + \boldsymbol{F}_I(t)\boldsymbol{d}]P.$$

This Hamiltonian determines the propagator $\tilde{U}_0(t_2,t_1)$ in Eq. (6).

In what follows we assume that the ir follows the xuv pulse. The xuv pulse is assumed to be restricted to the time interval from $t = 0$ to $t = T_X$ and the ir pulse to the interval from $t = \delta$ to $t = \delta + T_I$ with $\delta > T_X$. The integration limit T in Eq. (6) is thus equal to $T = \delta + T_I$; δ can be viewed as the ir pulse delay with respect to the xuv pulse with time zero indicating synchronicity of the xuv and ir pulses [see Fig. 1(b)]. Equation (6) for the transition amplitude then can be rewritten as

$$a_{(\lambda,\epsilon)}(\delta + T_I) \approx -e^{-i\epsilon T_I}\sum_{i=2}^{n} e^{-iE_i\delta}A_i(\lambda,\epsilon) \tag{7}$$

with

$$\begin{aligned} A_i(\lambda,\epsilon) = [\tilde{\boldsymbol{F}}_X(E_i - E_0)\boldsymbol{d}_{i,0}]\sum_{j=2}^{n}\int_\delta^{\delta+T_I} dt'\, e^{i\epsilon(t'-\delta)} \\ \times[\boldsymbol{F}_I(t')\boldsymbol{d}_{(\lambda,\epsilon),j}]\langle\phi_j|\tilde{U}_0(t',\delta)|\phi_i\rangle. \end{aligned} \tag{8}$$

In the derivation of this expression, only the justifiable assumption was made that photoionization of the atomic state ϕ_1 by absorption of one ir photon can be neglected [see Fig. 1(a)]. In the amplitude $A_i(\lambda,\epsilon)$ in Eq. (8),

$$\tilde{\boldsymbol{F}}_X(\omega) = \int_{-\infty}^{\infty} dt\, e^{i\omega t}\boldsymbol{F}_X(t)$$

is the Fourier transform of the xuv pulse evaluated at the individual transition frequencies $\omega_i = E_i - E_0$ from the atomic ground state to the respective excited state ϕ_i. The remaining integral in Eq. (8) involves the ir laser-pulse-driven dynamics in the intermediate bound states via the matrix elements of the propagator $\tilde{U}_0(t',\delta)$ (with $\tilde{U}_0(\delta,\delta) = \mathbf{I}$). In modeling our experimental data we calculate the temporal evolution of these matrix elements numerically by taking into account the relevant excited bound states. Despite its occurrence in the integration limits in Eq. (8), the value of the integral does not depend on the delay δ. The final continuum amplitudes $a_{(\lambda,\epsilon)}(\delta + T_I)$ depend on δ only via the exponentials $\exp(-iE_i\delta)$, i.e., via the unperturbed evolution of the excited bound states in between the two laser pulses.

In the most simple situation, the ir laser pulse does not modify the intermediate state dynamics but only serves to ionize the system. In this case the matrix elements of the propagator $\tilde{U}_0(t',\delta)$ reduce to their unperturbed values given by

$$\langle\phi_j|\tilde{U}_0(t',\delta)|\phi_i\rangle = \delta_{i,j}\exp[-iE_i(t' - \delta)].$$

Consequently, the amplitude $A_i(\lambda,\epsilon)$ in Eq. (8) at the end of the pulse sequence is simply given by

$$A_i(\lambda,\epsilon) = [\tilde{\boldsymbol{F}}_I(\epsilon - E_i)\boldsymbol{d}_{(\lambda,\epsilon),i}][\tilde{\boldsymbol{F}}_X(E_i - E_0)\boldsymbol{d}_{i,0}]. \tag{9}$$

Here $\tilde{\boldsymbol{F}}_I(\omega)$ is the Fourier transform of the ir pulse evaluated at the transition frequencies $\epsilon - E_i$ from the intermediate state i to the final continuum state with energy ϵ. The photoelectron-kinetic-energy distribution corresponding to Eq. (7) is given by $|a_{(\lambda,\epsilon)}(\delta + T_I)|^2$. In this simple case, the distribution depends on the delay δ of the ir with respect to the xuv pulse in those regions of the photoelectron spectrum where the product $|\tilde{\boldsymbol{F}}_I(\epsilon - E_i)||\tilde{\boldsymbol{F}}_I(\epsilon - E_j)|$ is different from zero for $i \neq j$ [see Eq. (9)]. These are just those regions where it is impossible to distinguish between the quantum paths from the initial state ϕ_0 to the final continuum state $\phi_{(\lambda,\epsilon)}$ via two of the intermediate states i or j with different energies $E_i \neq E_j$. Depending on the electron kinetic energy ϵ, different periods $2\pi/|E_j - E_i|$ in the delay dependence of the electron yield, the quantum beats, may be found according to the intermediate states involved.

This simple quantum beat structure in the photoelectron spectrum becomes significantly modified when the ir laser pulse influences the bound-state dynamics with increasing light-pulse intensity. Now Eq. (7) determines the structure. Accordingly, the continuum quantum beats map the laser-driven bound-state dynamics to the photoelectron spectrum.

The kinetic energy distribution can thus be used to get insight into the bound-state dynamics. According to Eq. (7) the photoelectron-kinetic-energy distribution $Y(\delta,\epsilon)$ is always of the form

$$Y(\delta,\epsilon) = \sum_{\lambda} |a_{(\lambda,\epsilon)}(\delta + T_I)|^2$$

$$\approx \sum_{\lambda} \sum_{i,j=2}^{n} e^{-i(E_j - E_i)\delta} A_i(\lambda,\epsilon) A_j^*(\lambda,\epsilon), \qquad (10)$$

i.e., a superposition of periodic functions in the delay δ (Fourier series) having periods $2\pi/|E_j - E_i|$ determined by the unperturbed energy differences of the bound excited states involved. The excited bound-state dynamics that is induced by the ir laser pulse is encoded in the Fourier coefficients $A_i(\lambda,\epsilon)A_j^*(\lambda,\epsilon)$ of the discrete Fourier series in Eq. (10). They depend sensitively on the intensity of the ir laser pulse, which modifies the intermediate bound-state dynamics. Thus, in a situation where the ir pulse couples the bound states $\phi_2, \ldots, \phi_n$ nearly resonantly to the state ϕ_1, ac Stark shifting of the bound states in the ir laser pulse as well as population transfers are mapped to the Fourier amplitudes.

Experimental access to bound-state dynamics via photoelectron spectroscopy is thus possible by measuring the dependence of the photoelectron-kinetic-energy distribution as a function of the delay between the pulse exciting the intermediate bound states and the one inducing the strong-field dynamics and serving as the photoionization pulse. The Fourier coefficients $A_i(\lambda,\epsilon)A_j^*(\lambda,\epsilon)$ can then be deduced by Fourier transformation of measured spectra $Y_e(\delta,\epsilon)$ with respect to the time delay δ. This Fourier transform will show sharp resonances at the quantum beat frequencies $|E_i - E_j|$. Their amplitudes are just the absolute values of the Fourier coefficients $A_i(\lambda,\epsilon)A_j^*(\lambda,\epsilon)$.

III. EXPERIMENTAL SETUP

We used a chirped-pulse amplified Ti:sapphire laser system, delivering pulses at a repetition rate of 3.3 kHz with a pulse width of 25 fs. The pulse central wavelength was 790 nm (1.57 eV) with a spectral width of 63 nm (0.125 eV) full width at half maximum (FWHM) (see the inset in Fig. 6).

Using a mirror with a drilled central hole, the laser beam was split into two parts. A central part with a diameter of 8 mm was carrying most of the energy (300 μJ per pulse). This pulse was used for high-order harmonic generation. The annular part with up to 60 μJ pulse energy was used as an infrared probe pulse. The delay between the two parts was controlled with a precision of $\approx$100 as by a motorized pair of silica glass wedges in the beam path of the central part. Behind the delay stage, both parts were recombined on a second mirror with a drilled central hole and propagated further collinearly.

An xuv pulse was generated through high-order harmonic generation by focusing the ir beam into a gas cell filled with krypton, using a lens with a focal length of 1.2 m. The krypton density was adjusted to efficiently generate harmonics up to order 15. The photon energy of the 13th harmonic (to be referred to as H13 hereafter), which is responsible for populating bound excited states of the neon atom, was centered at 20.4 eV. It had an estimated spectral width of 0.4 eV FWHM.

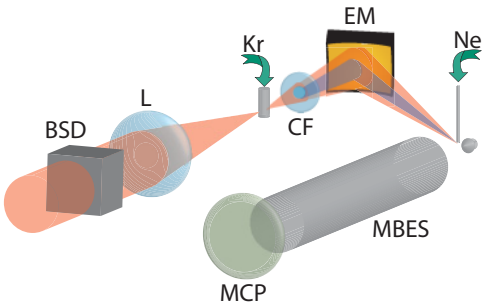

FIG. 2. (Color online) Schematic view of the experimental setup: BSD, beam splitting and delay stage; L, focusing lens; CF, combined xuv-ir filter; EM, grazing incidence elliptic mirror; MBES, magnetic bottle electron spectrometer; MCP, microchannel plate detector for the photoelectrons.

Subsequently, separation of the xuv from the generating ir beam was accomplished by a combined aluminum-glass filter. It consisted of a 200-nm-thick aluminum foil with 4.5 mm in diameter, which completely blocked the ir radiation from the central part of the beam. Additionally, any xuv radiation below 15 eV photon energy (ninth harmonic and less) was stopped by the foil. Annularly surrounding this foil, a 200-μm-thick BK-7 glass plate was installed to block any overly divergent xuv radiation and pass the annular ir probe beam. The xuv and probe ir radiation were then focused by a gold-coated elliptic grazing incidence mirror into an effusive jet of neon gas. The kinetic energy of photoelectrons resulting from ionization of that gas was measured in a magnetic bottle-type time-of-flight spectrometer. A schematic view of the setup is shown in Fig. 2.

The delay imposed by the glass part of the combined filter on the ir probe, yet not on the xuv pulses, ensured that the harmonic-generating part of the ir beam and the probe part did not overlap temporally at the source point for harmonic generation when the xuv and ir probe pulses overlapped in time within the magnetic bottle spectrometer. Moreover, it was possible to delay the ir probe with respect to the xuv pulse by up to 750 fs before interfering with the harmonic generation. A second, wider accessible delay range with no interference with the harmonic generation started at a delay of the ir pulse of 1100 fs with respect to the xuv pulse.

IV. EXPERIMENTAL RESULTS

Figure 3 shows the dependence of the kinetic energy distribution of the observed photoelectrons on the xuv-ir pulse delay after application of the pulse sequence to the neon atom in a grayscale two-dimensional plot. The kinetic energy range shown, from 0 to 4 eV, covers photoelectrons resulting from direct photoionization by harmonic H15 at an excess energy of $\approx$2 eV as well as electrons with kinetic energies separated by one ir photon energy from these. The delay between the two pulses ranges from -50 to 200 fs, with positive delays referring to the ir following the xuv pulse. From the predominant structure in this plot, the narrow maximum close to 2 eV, the overlap in time of the two pulses can be easily identified. In the case of temporal overlap a slight reduction in kinetic energy of the photoelectrons appears. This is due to

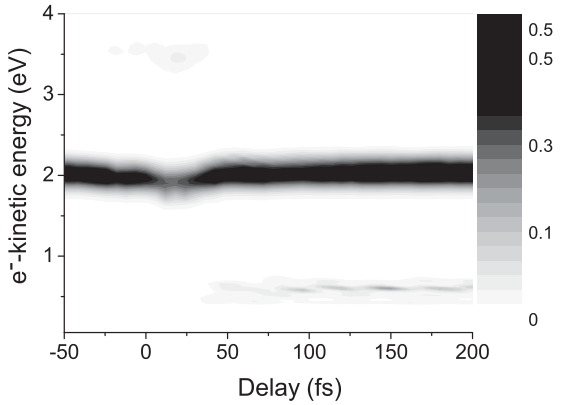

FIG. 3. Two-dimensional plot of the photoelectron yield as a function of the delay δ and the photoelectron kinetic energy. Clearly visible is the delay range where the two pulses overlap in time. Here the kinetic energy of the photoelectrons originating from photoionization of Ne by the harmonic H15 around 2 eV slightly decreases. Around 0.6 eV the two-step ionization mechanism shown in Fig. 1 via intermediate bound Ne states contributes for positive delay settings.

a small ponderomotive rising of the Ne ionization threshold through the ultrashort, high-intensity ir laser pulse (pulse peak intensity in this case is $\approx$2.2 TW/cm^2) [7]. The simultaneous reduction in the electron yield is due to the redistribution of photoelectrons in the spectrum because of formation of sidebands while the xuv and ir pulses overlap in time [8].

The second salient feature in Fig. 3, which is in the focus of this investigation, is an onset of ionization around 0.6 eV photoelectron kinetic energy when the ir follows the xuv pulse, i.e., for positive delays. These photoelectrons originate from photoionization of bound excited neon states that have before been populated by absorption of one H13 photon from the xuv beam. The bound states that can be populated through a dipole-allowed transition from the ground state by the H13 part of the xuv pulse are compiled in Table I. For the sake of brevity we frequently use the shortcut notations 2-5, also given in the table, when referring to these states. They all have a total angular momentum of $J = 1$ and are photoionized by absorption of one further photon of the applied ir probe laser pulse.

For a detailed examination of this ionization channel, we have chosen xuv-ir pulse delay settings starting at 1100 fs and ranging up to 2250 fs, which was the maximum range accessible to our experimental setup. For these settings the xuv pump and ir probe pulses were temporally separated in the harmonic generation cell, thus avoiding interference of the ir probe pulse with the harmonic generation. A detailed grayscale two-dimensional plot of the energy-resolved photoelectron yield for this range of delay times is shown in Fig. 4(a) in the kinetic energy range between 0.3 and 0.9 eV. The figure reveals an intricate delay-time-dependent structure in the photoelectron-kinetic-energy distribution that is caused by the quantum beat oscillations introduced in Sec. II. Figure 4(b) gives a quantitative impression of the dependence of the total photoelectron yield in the energy range from 0.3 to 0.9 eV on the delay δ. Similar to the delay dependence of the kinetic energy distribution, also the total photoelectron yield shows the quantum beat structure. Since several quantum paths via the bound excited Ne states interfere (see Table I), no completely regular oscillation structure is found in the total photoelectron yield.

TABLE I. Overview of the excited states in neon relevant in the experiment, their respective excitation energies from the Ne ground state [9], and the shortcut notations used in this paper.

Shortcut	Configuration	Term	J	Energy (eV)
1	$2s^2 2p^5 (^2P^o_{1/2}) 3p$	$^2[1/2]^o$	0	18.966
2	$2s^2 2p^5 \left(^2P^o_{3/2}\right) 5s$	$^2[3/2]^o$	1	20.571
3	$2s^2 2p^5 \left(^2P^o_{1/2}\right) 5s$	$^2[1/2]^o$	1	20.663
4	$2s^2 2p^5 \left(^2P^o_{3/2}\right) 4d$	$^2[1/2]^o$	1	20.702
5	$2s^2 2p^5 \left(^2P^o_{3/2}\right) 4d$	$^2[3/2]^o$	1	20.709

In the experiment, the ir intensities have been kept at a level so as to avoid strong-field effects on the ionization step of the bound excited states that were populated by the xuv laser pulse. In fact we find a linear relation between the cumulated photoelectron yield in the kinetic energy range between 0.3 and 0.9 eV and the ir probe pulse intensity, as Fig. 5 shows. This confirms that it is feasible to approximate the ir photoionization step perturbatively. The theoretical analysis presented in Sec. II relies on this experimental finding.

Two photoionization channels, the $\mathrm{Ne}^{+2P}_{3/2}$ (ionization potential $I_p = 21.5654$ eV) and the $\mathrm{Ne}^{+2P}_{1/2}$ ($I_p = 21.6613$ eV) channels, are open after absorption of one H13 and one ir photon. In order to reveal the different contributions to the photoelectron-kinetic-energy distribution, Fig. 6 shows a cut through Fig. 4(a) at a specific delay ($\delta = 1750$ fs). Above the photoelectron spectrum the numbered marks on the two lines drawn indicate the kinetic energies where one expects to detect photoelectrons in the respective ionization channel after ir photoionization of intermediate bound states 2-5. Since these bound states all have a total angular momentum of $J = 1$, the final continuum states reached must have $J = 0$ or $J = 2$. The $J = 1$ ionization continuum cannot be reached since the directions of polarization of the ir and the xuv beams are parallel [10,11]. For any of the individual intermediate states there are further restrictions concerning the ionization continuum that can be reached; however, neither of these is strict. For every intermediate state we have collected the accessible ionization continua in Table II. The notation in the table assumes the jl coupling scheme for noble gases with the intermediate angular momentum quantum number K given in square brackets (see, for example, [10]). Primarily, the photoelectron can be left with two angular momentum quantum numbers, $l = 1$ or $l = 3$, that cannot be distinguished experimentally with a magnetic bottle spectrometer. The main ionization channels for each intermediate state are highlighted with bold letters. This assertion is based on the supposition that the respective bound state and the ionization continua have well-defined core states (^2P_j with $j = 1/2$ or $j = 3/2$), which are not changed in the ionizing transition.

From the photoelectron-kinetic-energy distribution in Fig. 6, the actual contributions of the different possible ionization channels cannot be directly extracted. As can be seen already from the width of the ir laser pulse spectrum shown in the inset of Fig. 6, the structures that appear in

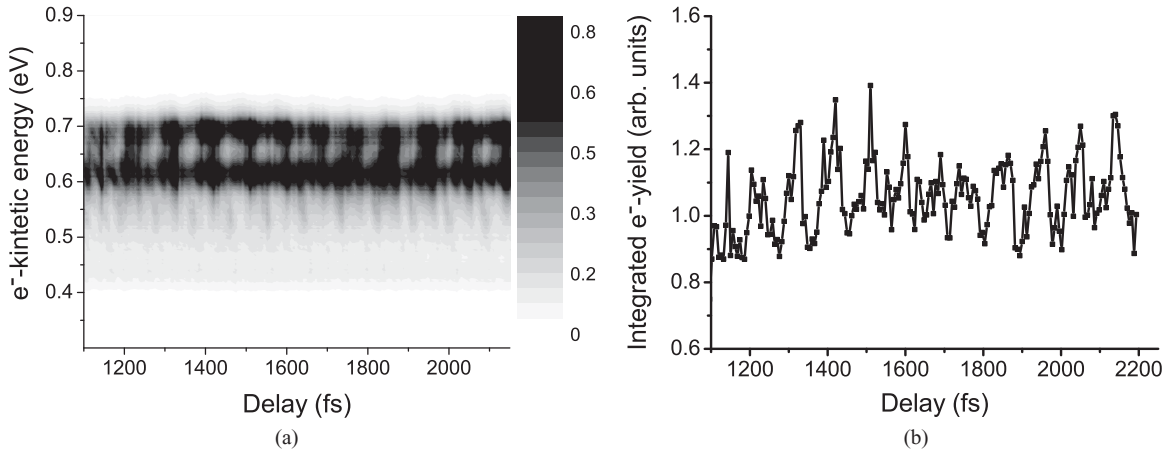

FIG. 4. (a) The xuv-ir delay dependence of the photoelectron-kinetic-energy distribution in the energy range 0.3 to 0.9 eV where photoelectrons result from the two-step ionization process of Ne. (b) Energy-integrated yield of the photoelectrons detected in the energy range 0.3 to 0.9 eV. The photoelectron spectra were taken in a delay range from 1100 to 2200 fs.

the photoelectron-kinetic-energy distribution are to a great deal not due to resolving the energy differences between intermediate bound states 2-5. The interference phenomena due to different possible quantum paths leading to the same final continuum state that were introduced in Sec. II are mainly responsible for the structure.

In order to quantify the oscillations of the photoelectron yield with the delay δ that can be observed in Fig. 4, we Fourier-transformed the cumulated photoelectron yield between 0.4 and 0.8 eV kinetic energy with respect to δ,

$$\tilde{Y}_e(\Omega) = \int_{\delta_0}^{\delta_1} d\delta\, e^{i\Omega\delta} \int_{0.4\,\mathrm{eV}}^{0.8\,\mathrm{eV}} d\epsilon\, Y_e(\delta,\epsilon),$$

using the limits of the delay scan in Fig. 4 as upper and lower limits for the time integration. Here $Y_e(\delta,\epsilon)$ denotes the measured delay-dependent photoelectron spectrum with ϵ being the photoelectron kinetic energy. The absolute value of the amplitude of the Fourier transform $|\tilde{Y}_e(\Omega)|$ is shown in Fig. 7. For easily establishing the connection to the energy spacings of the involved intermediate bound states, the Fourier frequency Ω has been converted to energy units in the plot. The range of delays of 1150 fs covered in the experiment allowed for an energy resolution in the Fourier frequency of ≈4 meV. As the energy separation of intermediate states 4 and 5 is only 7 meV, some peaks are not completely resolved. However, six peaks in total are discernible at precisely the energy-level differences $|E_i - E_j|$ of all combinations of the involved intermediate states. They can be attributed to quantum beat oscillations stemming from ionization pathways via excited bound-state pairs [see Eq. (10)]. The respective state pairs are indicated in the graph, using the notation i-j to name the two states involved (i and j being the shortcut state notations from Table I). The quasidiscrete structure that is found in the Fourier transform at the expected energies corroborates that the quantum beat mechanism introduced in Sec. II actually causes the observed oscillations.

The appearance of a specific line i-j in the Fourier spectrum in Fig. 7 indicates that the same final continuum state can

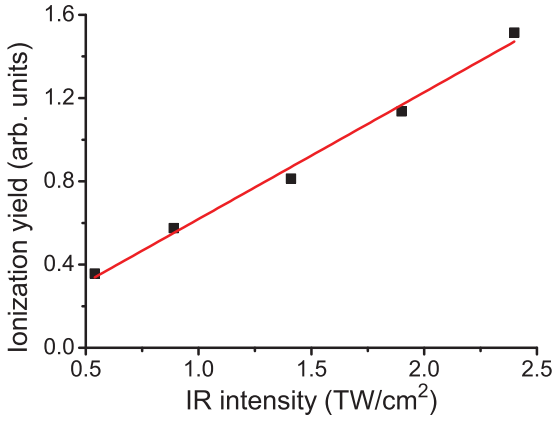

FIG. 5. (Color online) The cumulated photoelectron yield in the energy region 0.3 to 0.9 eV plotted vs the ir probe pulse intensity. In the intensity range used, the yield depends linearly on the ir light intensity.

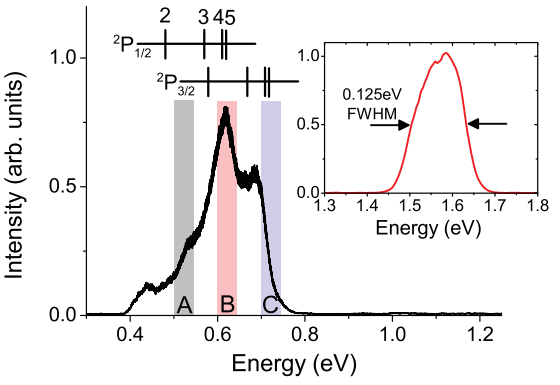

FIG. 6. (Color online) Sample photoelectron spectrum for a fixed xuv-ir delay setting of $\delta = 1750$ fs. The marks at the top with labels 2-5 indicate the excess energy that photoelectrons have when they are promoted to the ionization continuum from excited bound states 2-5 by absorption of one ir photon (energy, 1.57 eV). This is indicated for both ionization channels $^2P_{1/2}$ and $^2P_{3/2}$. The boxes A, B, and C indicate the energy intervals used for integration in Fig. 8. The inset shows the measured spectrum of the ir laser pulse.

TABLE II. Final continua reached by photoionization of the bound excited states 2-5 in Table I. Continua with total angular momentum $J = 0,2$ can be reached with the ion core left either in the $^2P_{3/2}$ ground or in the $^2P_{1/2}$ excited state. The photoelectron may have either angular momentum $l = 1$ (ϵp continuum) or $l = 3$ (ϵf continuum) with ϵ its kinetic energy. The expressions in brackets give the K angular momentum quantum number according to the jl coupling scheme for noble gas atoms (see, for example, [10]). Bold letters highlight those continua that can be reached without changing the core state of the neon atom in the ionizing transition.

Initial		Final	
Shortcut	$J = 1$	$J = 0$	$J = 2$
2	$(^2\boldsymbol{P}^o_{3/2})5s[3/2]$	$(^2\boldsymbol{P}^o_{3/2})\epsilon\,\boldsymbol{p}[\boldsymbol{1/2}]$, $(^2\boldsymbol{P}^o_{1/2})\epsilon\,\boldsymbol{p}[1/2]$	$(^2\boldsymbol{P}^o_{3/2})\epsilon\,\boldsymbol{p}[\boldsymbol{3/2}]$, $(^2\boldsymbol{P}^o_{3/2})\epsilon\,\boldsymbol{p}[\boldsymbol{5/2}]$, $(^2\boldsymbol{P}^o_{1/2})\epsilon\,\boldsymbol{p}[3/2]$
3	$(^2\boldsymbol{P}^o_{1/2})5s[1/2]$	$(^2\boldsymbol{P}^o_{3/2})\epsilon\,\boldsymbol{p}[1/2]$, $(^2\boldsymbol{P}^o_{1/2})\epsilon\,\boldsymbol{p}[\boldsymbol{1/2}]$	$(^2\boldsymbol{P}^o_{3/2})\epsilon\,\boldsymbol{p}[3/2]$, $(^2\boldsymbol{P}^o_{3/2})\epsilon\,\boldsymbol{p}[5/2]$, $(^2\boldsymbol{P}^o_{1/2})\epsilon\,\boldsymbol{p}[\boldsymbol{3/2}]$
4	$(^2\boldsymbol{P}^o_{3/2})4d[1/2]$	$(^2\boldsymbol{P}^o_{3/2})\epsilon\,\boldsymbol{p}[\boldsymbol{1/2}]$, $(^2\boldsymbol{P}^o_{1/2})\epsilon\,\boldsymbol{p}[1/2]$	$(^2\boldsymbol{P}^o_{3/2})\epsilon\,\boldsymbol{p}[\boldsymbol{3/2}]$, $(^2\boldsymbol{P}^o_{3/2})\epsilon\,\boldsymbol{p}[\boldsymbol{5/2}]$, $(^2\boldsymbol{P}^o_{1/2})\epsilon\,\boldsymbol{p}[3/2]$
			$(^2\boldsymbol{P}_{3/2})\epsilon\,\boldsymbol{f}[\boldsymbol{3/2}]$, $(^2\boldsymbol{P}_{3/2})\epsilon\,\boldsymbol{f}[\boldsymbol{5/2}]$, $(^2\boldsymbol{P}_{1/2})\epsilon\,\boldsymbol{f}[5/2]$
5	$(^2\boldsymbol{P}^o_{3/2})4d[3/2]$	$(^2\boldsymbol{P}^o_{3/2})\epsilon\,\boldsymbol{p}[\boldsymbol{1/2}]$, $(^2\boldsymbol{P}^o_{1/2})\epsilon\,\boldsymbol{p}[1/2]$	$(^2\boldsymbol{P}^o_{3/2})\epsilon\,\boldsymbol{p}[\boldsymbol{3/2}]$, $(^2\boldsymbol{P}^o_{3/2})\epsilon\,\boldsymbol{p}[\boldsymbol{5/2}]$, $(^2\boldsymbol{P}^o_{1/2})\epsilon\,\boldsymbol{p}[3/2]$
			$(^2\boldsymbol{P}_{3/2})\epsilon\,\boldsymbol{f}[\boldsymbol{3/2}]$, $(^2\boldsymbol{P}_{3/2})\epsilon\,\boldsymbol{f}[\boldsymbol{5/2}]$, $(^2\boldsymbol{P}_{1/2})\epsilon\,\boldsymbol{f}[5/2]$

be reached via these two states. The final continuum state is determined by the final ionic state and the state of the free photoelectron. In the case of the low-energy line 4-5, photoionization can obviously reach the same final continuum states (see Table II). Both bound states have the same ion core $^2P_{3/2}$, and the excited electron is a $4d$ electron in both cases. Ionization into the final continua ($^2P_{3/2}\,\epsilon p$) and ($^2P_{3/2}\,\epsilon f$) without changing the ion core configuration contributes to this quantum beat line. Also, core-changing transitions may contribute, however, possibly to a lower extent. The lines 2-3, 3-4, and 3-5 also appear in the Fourier-transform spectrum (Fig. 7). For these lines core-changing transitions are definitely necessary, since bound state 3 has a $^2P_{1/2}$ and the others have a $^2P_{3/2}$ ion core. It is only such a transition that allows reaching the necessary identical final state. A core-changing transition in the ionization step may have two possible reasons. Either the excited bound states involved do not have a unique ion core state, or the nearly resonant coupling of the group of states 2-5 to state 1 ($^2P_{1/2}\,3p$) via the ir laser pulse efficiently mixes the two core states. This point is discussed in more detail below in connection with the kinetic-energy-resolved Fourier spectra.

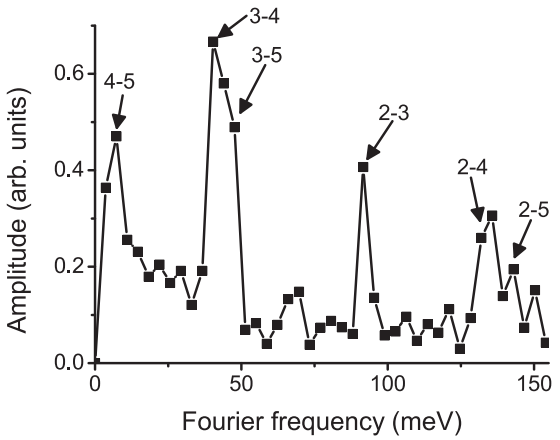

FIG. 7. Fourier transform of the cumulated photoelectron yield in the energy range 0.4 to 0.8 eV from the measurement in Fig. 4.

The same discrete line structures that appear in the energy-integrated Fourier transform of Fig. 7 can also be found in photoelectron-kinetic-energy-resolved Fourier transforms

$$\tilde{Y}_e(\Omega,\epsilon) = \int_{\delta_0}^{\delta_1} d\delta\; e^{i\Omega\delta}\; Y_e(\delta,\epsilon)$$

of the xuv-ir delay-dependent photoelectron spectra. In any subinterval within the kinetic energy range of interest, from 0.4 to 0.8 eV, these structures appear at the same beat frequencies $\Omega = |E_i - E_j|$. The line intensities $|\tilde{Y}_e(|E_i - E_j|,\epsilon)|$, however, depend sensitively on the photoelectron kinetic energy ϵ. This dependence can immediately be seen in the Fourier spectra derived from the experimental data in Figs. 8(a), 8(c), and 8(e). In the latter sequence, the ir probe pulse peak intensity has been varied. The light intensities used are 0.5, 0.9, and 1.3 TW/cm^2, respectively. In each graph in the figure, we show the amplitude $|\tilde{Y}_e(\Omega,\epsilon)|$ of the Fourier transform with respect to the delay δ in three photoelectron-kinetic-energy intervals. These intervals [0.5 eV, 0.55 eV], [0.6 eV, 0.65 eV], and [0.7 eV, 0.75 eV] are referred to by capital letters A, B, and C, respectively. They are also indicated as boxes in Fig. 6. As can be seen from the marks at the top of that graph, the energy intervals have been chosen such that, in interval A, primarily the 2-3 beating in the $^2P_{1/2}$ ionization channel should contribute, while in interval C the 4-5 beating in the $^2P_{3/2}$ channel should prevail. In the central interval B, all beating frequencies are expected to occur.

According to Table II we expect to find the 4-5 quantum beat at 7 meV at all ir light intensities, particularly also for vanishing intensities, since identical final continuum states in the $^2P_{3/2}$ ionization channel can always be reached in the ionization transition from either intermediate state 4 or 5. In the experimental spectra in Fig. 8 this is confirmed. The beating is present at all investigated intensities and appears most pronounced in the kinetic-energy intervals B and C, whereas the amplitude vanishes in interval A. This behavior is independent of the ir light intensity in the range we investigated. It is striking that the amplitude peaks in interval B at low ir light intensity, whereas it becomes increasingly pronounced with intensity in interval C.

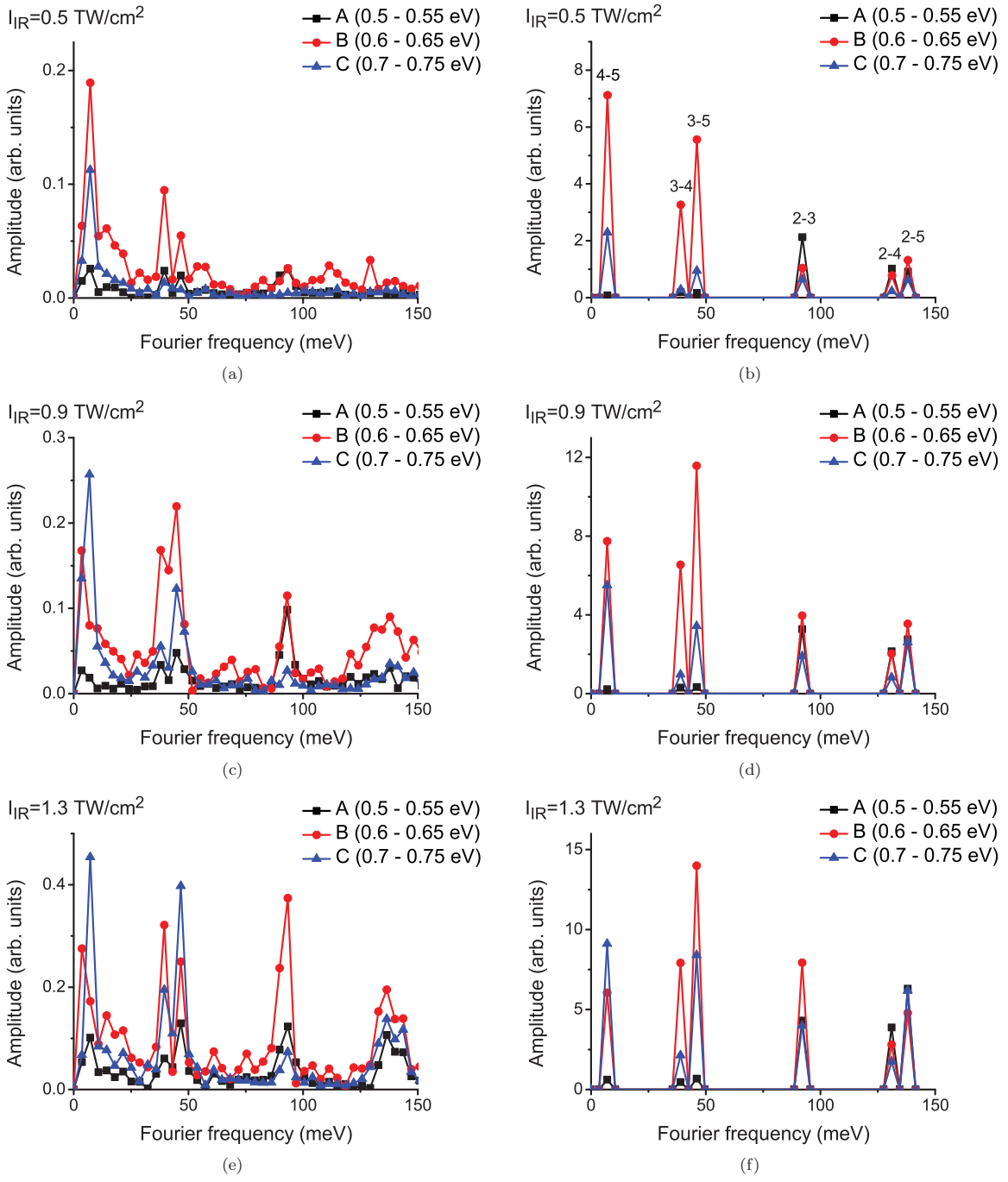

FIG. 8. (Color online) (a, c, e) Fourier transforms of the oscillating electron yield for different intervals of photoelectron kinetic energy and different ir pulse intensities. For the position of the intervals within the photoelectron spectrum, see Fig. 6. (b, d, f) Results of the model calculation of the amplitudes of the quantum beat oscillations obtained for the same parameters that were used in the experiment for comparison. In (b) each peak is provided with the notation i-j to name the two intermediate states responsible for the corresponding quantum beat. This assignment can be transferred to all other spectra shown here.

At first glance the appearance of 2-3 quantum beats in the experimental Fourier spectra in Fig. 8 at 92 meV is unexpected as the intermediate states 2 and 3 have differently coupled ion cores ($^2P_{3/2}$ and $^2P_{1/2}$, respectively) with the excited electron in the 5s state. Only a negligible admixture of $^2P_{1/2}$ 5s character in state 2 is expected [12]. According to Table II, one thus expects that ionization of these states exclusively ends up in differing final continuum states. Indistinguishable quantum paths, the prerequisite for quantum beats to appear, thus seemingly do not exist. In the experimental spectra, the 2-3 beat amplitude is weak at the lowest ir intensity [Fig. 8(a)] and appears only in the low-kinetic-energy interval A. However, the amplitude increases strongly with the light intensity and appears distributed over the whole kinetic energy distribution, with the maximum amplitude found in the central kinetic-energy interval B. This beat structure thus seems to be induced by the ir field. It couples both intermediate states 2 and 3 to state 1 with a $^2P_{1/2}$ ion core during photoionization (see

Table I). This admixture enables reaching the $^2P_{3/2}$ ionization continuum also from intermediate state 3, thus inducing quantum beat oscillations. This point is further discussed below in conjunction with our model calculation.

For the same reasons as with the 2-3 quantum beat structure, one does not expect the 3-4 and 3-5 structures to appear in the Fourier transform spectra (Fig. 8). Nevertheless, they are readily found in the spectra at 39 and 46 meV Fourier frequency, respectively. As they also show a sensitive dependence on the ir light intensity, with the tendency to disappear for low light intensity, they also seem to be induced by a mixing of bound states by the ir laser pulse during photoionization.

The 2-4 and 2-5 beat structures show a similar behavior as the 2-3 beating, being almost absent in the low-ir-intensity measurement in Fig. 8(a) and becoming more pronounced relative to the other structures with increasing intensity. At first glance this seems to contradict our model, since all involved intermediate states have a $^2P_{3/2}$ ion core and can thus end up in the same ionization channel. Analogous to the 4-5 beating, one would therefore expect quantum beats to occur, even at low ir pulse intensities. However, the 2-4 and 2-5 energy separations are 131 and 138 meV, respectively (see Table I). This is larger than the FWHM of the ir laser pulse (125 meV, see Fig. 6). The spectral overlap of the photoelectron distributions starting from these states is thus small, and the associated quantum beats in the low-ir-intensity limit is correspondingly weak. With increasing ir intensity the coupling to state 1 facilitates ac Stark shifts, which may lead to a smaller energy separation of the states in turn. Also mixing of the bound states may occur, similar as with the 2-3, 3-4, and 3-5 beat amplitudes. These effects may therefore explain the more pronounced occurrence of the 2-4 and 2-5 quantum beats at higher ir intensity.

V. COMPARISON WITH MODEL CALCULATION

Within the model developed in Sec. II, we can identify the photoelectron-kinetic-energy-resolved Fourier line intensities $|\tilde{Y}_e(|E_i - E_j|,\epsilon)|$ derived from the experimental data with the theoretically derived Fourier coefficients $A_i(\lambda,\epsilon)A_j^*(\lambda,\epsilon)$ appearing in Eq. (10) via

$$\left|\sum_\lambda A_i(\lambda,\epsilon)A_j^*(\lambda,\epsilon)\right| \propto |\tilde{Y}_e(|E_i - E_j|,\epsilon)|.$$

The sum over λ extends over all open final ionization channels. According to this relation, the sensitive dependence of the experimentally determined amplitudes of the quantum beat oscillations on the ir laser intensity becomes obvious. The theoretically derived amplitudes $A_i(\lambda,\epsilon)$ are affected by the possible coupling of the group of bound states excited by the xuv pulse to other bound states through the ir photoionization laser pulse [see Fig. 1(a)]. Through these couplings the ir laser pulse modifies the excited-state wave packet while ionizing it. As the experiment corroborates, this modification may create new indistinguishable quantum paths to the final continuum states, which in turn give rise to new quantum beat oscillations. These are expected to vanish in the limit of negligible ir light intensity.

The computer simulation of the investigated process implements the model outlined in Sec. II. It thus involves the coupling of the wave packet excited by the xuv pulse to lower-lying bound states. For such a coupling to be efficient at the ir intensities used in our experiments, a coupled state needs to be separated from states 2-5, of which the wave packet is composed, by roughly one ir photon energy (1.57 eV). The states populated by the xuv pulse all have a total angular momentum of $J = 1$. Since the ir and xuv beams are polarized parallel with respect to each other, the only possible candidates for the coupling are excited states $(^2P_j)3p$ with an ion core with $j = 1/2$ or $j = 3/2$ and a total angular momentum of either $J = 0$ or $J = 2$ [10,11]. Altogether five $3p$ states qualify for these criteria. However, only for the $(^2P_{1/2})3p[1/2]$ state with $J = 0$, which is listed in Table I with shortcut notation 1, a partial overlap of the transition frequencies to states 2-5 with the spectrum of the ir laser pulse exists. Due to the more pronounced off-resonance character, the influence of the other four $3p$ states is expected to be much smaller. Therefore only this state is incorporated in the model calculation. Although state 1 has a $^2P_{1/2}$ ion core, it has nonzero transition dipole matrix elements to all states 2-5, i.e., also to those with ion core $^2P_{3/2}$ [13]. This fact and a quantum defect analysis by Starace [12] indicate that the $(^2P_{1/2})3p[1/2]$, $J = 0$ state does not have a pure $^2P_{1/2}$ ion core but admixtures of $^2P_{3/2}$ character. On the other hand, states 2-5 are expected to have quite pure ion cores [12,14] with either $j = 3/2$ or $j = 1/2$.

The Hamiltonian matrix consisting of the four states 2-5 and the lower state 1 (see also Table I) as well as the coupling of the intermediate states to state 1 that is induced by the ir laser pulse is given by

$$\tilde{H}_0(t) = \begin{pmatrix} E_1 & \mathbf{F}_I(t)\,\mathbf{d}_{1,2} & \mathbf{F}_I(t)\,\mathbf{d}_{1,3} & \mathbf{F}_I(t)\,\mathbf{d}_{1,4} & \mathbf{F}_I(t)\,\mathbf{d}_{1,5} \\ \mathbf{F}_I(t)\,\mathbf{d}_{2,1} & E_2 & 0 & 0 & 0 \\ \mathbf{F}_I(t)\,\mathbf{d}_{3,1} & 0 & E_3 & 0 & 0 \\ \mathbf{F}_I(t)\,\mathbf{d}_{4,1} & 0 & 0 & E_4 & 0 \\ \mathbf{F}_I(t)\,\mathbf{d}_{5,1} & 0 & 0 & 0 & E_5 \end{pmatrix}. \quad (11)$$

This Hamiltonian determines the evolution in time of the corresponding bound-state wave packet while the ir ionizing laser pulse is applied. The dipole matrix elements $\mathbf{d}_{i,1}$ appearing in $\tilde{H}_0(t)$ are assumed to be real.

The time-dependent Schrödinger equation for the propagator matrix $\tilde{U}_0(t,\delta)$ corresponding to the Hamiltonian $\tilde{H}_0(t)$ is solved numerically, using for each time step $t \to t+\delta t$ the unitary propagator

$$\left[i + \frac{\delta t}{2}\tilde{H}_0\left(t+\delta t/2\right)\right]\left[i - \frac{\delta t}{2}\tilde{H}_0\left(t+\delta t/2\right)\right]^{-1}. \quad (12)$$

This approximates the exact propagator $\tilde{U}_0(t+\delta t,t)$ for each time step [15]. With the so-determined matrix elements of the propagator, the transition amplitude from the atomic ground state ϕ_0 to the final continuum states characterized by a photoelectron kinetic energy ϵ was then determined using Eqs. (7) and (8). This step needs to be carried out independently for each possible ionization channel. As discussed in Sec. IV we assumed that the ion core coupling of bound states 2-5 is not changed in the ionizing transition and that no coupling of ionization channels with different ion core exists. We also replaced the ionization channels listed in Table II by two effective ionization channels, one with ion core $^2P_{3/2}$ and one with $^2P_{1/2}$. These are model assumptions made to reduce the complexity of the calculation. The assumptions made imply that we set the transition dipole matrix elements $\boldsymbol{d}_{(\lambda,\epsilon),j}$ in Eq. (8) for bound states 2, 4, and 5 to zero when calculating ionization into the $^2P_{1/2}$ channel and similarly for state 3 when calculating ionization into the $^2P_{3/2}$ channel. The photoelectron-kinetic-energy distributions that we calculate in this way have to be added up incoherently to determine the total distribution. The quantum beat amplitudes at the beat frequencies $|E_j - E_i|$ are then given by $|\sum_\lambda A_i(\lambda,\epsilon)A_j^*(\lambda,\epsilon)|$ [see Eq. (10)]. They correspond to the respective experimentally determined quantum beat oscillation amplitudes $|\tilde{Y}_e(|E_i - E_j|,\epsilon)|$. The entire procedure was repeated for different values of the ir pulse peak intensity, which enters in Eqs. (8) and (11) via the electric ir field strength $\boldsymbol{F}_I(t)$. The intensities used in the calculations matched the ones employed in the experiment.

The numerical simulation needed the input of several parameters, which were chosen according to the following considerations. For the temporal envelope of the ir pulse we assumed the function

$$\overline{\boldsymbol{F_I}}(t) = \sin^2\left(\frac{\pi\, t}{T_I}\right), \quad t \in [0, T_I].$$

The duration T_I was set to 68 fs, corresponding to a FWHM in intensity of the pulse of 25 fs, which matched the pulse width of the ir pulse used in the experiments. The transition dipole matrix elements $\boldsymbol{d}_{1,j}$ needed to quantify the Hamiltonian in Eq. (11) are unknown. However, theoretically determined values for the respective oscillator strengths are given in [13]. From these we determined the absolute values of one of the Cartesian components of the $\boldsymbol{d}_{1,j}$. In the model calculation we then used these absolute values. Since they were not accessible, possible phases have been neglected. A rather large uncertainty enters through the choice of the amplitudes for bound states 2-5 in the bound-state wave packet with which to start the propagation in time. They are determined by the transition matrix elements from the ground state to the respective excited states as well as by the spectral distribution of the xuv pulse [see Eq. (8)]. The transition matrix elements can also be taken from [13]. However, the spectral xuv intensity distribution can only be estimated. We therefore assumed starting amplitudes based on an xuv spectral intensity distribution estimated from a measured photoelectron spectrum from single-photon ionization of Ar atoms using the harmonic H13. Starting with this basic choice, we varied the xuv spectral distribution to best approximate the experimental data. The best qualitative agreement was found for the following choice of the spectral amplitudes $\tilde{F}_X(E_i - E_0)$ of the xuv H13 pulse: 0.32 ($i = 2$), 0.28 ($i = 3$), and 0.2 ($i = 4,5$). Here, we have chosen the arbitrary normalization that the $\tilde{F}_X(E_i - E_0)$ add up to 1.

The results of the numerical simulation are presented in Figs. 8(b),8(d), and 8(f) face to face with the experimental data for the three different peak intensities used in the experiments. The comparison shows a remarkable overall qualitative agreement. Minor deviations are expected given the specific simplifications and estimations that were assumed here. Specifically, the first peak at 7 meV beat frequency (the 4-5 beat amplitude) shows exactly the same behavior in both the experimental and the simulated spectra. This beating is most pronounced in the central kinetic-energy interval B of the photoelectron-kinetic-energy distribution at low ir light intensity, with a shift toward the high–energy side C at higher intensities. Similarly, for the double peak structure between 39 and 46 meV beat frequency (the 3-4 and 3-5 beat amplitudes), the predominant contributions at 0.5 TW/cm^2 are found in interval B. As also observed in the experiments, these oscillations become more pronounced in interval C with increasing ir intensity, though this increase is not as rapid in the simulation as it is in the experiments. The relative heights of the 3-4 and the 3-5 peaks are reproduced correctly in energy interval C. In interval B, however, this ratio appears reversed in the experiments. Similar to the experimental finding, the model calculation gives rise to significant 3-4 and 3-5 beat amplitudes already at the lowest ir light intensity [Figs. 8(a) and 8(b)], despite the fact that in the calculation we assumed that ionization of a state with core angular momentum j can only terminate in a continuum with the same ion core angular momentum. This means that the calculated quantum beat amplitudes 3-4 and 3-5 vanish for the ir intensity approaching zero. The result of the model calculation indicates that the coupling of states 3, 4, and 5 to state 1 via the ir laser field with the accompanying $j = 1/2, 3/2$ core state mixing suffices to account for the appearance of the 3-4 and 3-5 quantum beats in the experiment already at the lowest light intensity.

The experimental 2-3 beat amplitude at 92 meV beating frequency is rather weak at 0.5 TW/cm^2 and appears equally pronounced in intervals A and B, while with increasing intensity a dramatic increase, especially in the kinetic energy interval B, is found. Also, in interval C, a small contribution emerges. In the simulation this beat amplitude appears already at low ir intensity slightly more pronounced than observed, yet the general behavior in all three energy intervals is reproduced very well. Similar to the increase of the 3-4 and 3-5 beat amplitudes in interval C with the ir light intensity, the increase of the 2-3 amplitude in interval B appears to be more rapid in the experiments than can be explained by the simulation. The physical reason for the absence of these beatings at low ir intensity is the differently coupled ion core of the states involved. As discussed in Sec. IV, they emerge with rising ir

intensity due to an amplitude transfer among bound states 2-5 induced by their coupling to state 1.

The 2-4 and 2-5 beating frequencies appear not very well resolved in the experimental spectra. In Figs. 8(c) and 8(e), however, they are identifiable, while in the low-ir-intensity measurement in Fig. 8(a) they are almost absent. Also in the simulations one can observe only weak quantum beat oscillations at these frequencies at 0.5 TW/cm^2 and a moderate increase at higher intensities. As previously discussed, the absence of these beatings at low ir intensity is due to the limited bandwidth of the ir pulse, while their increase at higher intensity is caused by effects that are induced by the coupling. This interpretation is supported by the simulation.

From the theoretical side, we expect that the assumptions made upon independent continuum channels with the ion core coupled to either $^2P_{3/2}$ or $^2P_{1/2}$ and upon reducing the actual number of channels to two should explain most of the deviations between the experiments and calculations. Despite these approximations, the overall qualitative agreement is already astonishingly good.

From the experimental side, possible reasons for deviations of the calculated beat amplitudes from the measured ones are uncertainties regarding the weighting of the different ionization channels, the spectral distribution of the xuv H13 light, deviations of the actual ir pulse shape from the assumed one, and also several not precisely known experimental parameters of the magnetic bottle spectrometer. To a certain degree the spectrometer performs spatial averaging since photoelectrons are always detected from a finite volume of space. Due to the focusing geometry, the ir pulse peak intensity is position dependent and varies over this volume. The incorporation of these effects into the simulation would require knowledge of the precise focusing conditions of both the ir and the xuv beams together with their overlap in space as well as the beam overlap with the detection volume of the spectrometer. Unfortunately, neither of these are precisely accessible.

VI. CONCLUSION

Summarizing, we investigated quantum beat phenomena found in the photoelectron-kinetic-energy distribution after photoionization of an atomic system by a laser-pulse sequence, with the first pulse starting a bound-state wave packet that is photoionized by a second high-intensity ultrashort pulse. The results show that the quantum beat amplitudes sensitively depend on the kinetic energy of the leaving photoelectron and on the light intensity of the photoionization laser pulse.

Altogether, the model we presented to analyze the observed phenomena is well adapted to describe the effects that the ionizing ir laser pulse has on the composition of the quantum beat oscillations in the investigated two-color ionization process. With the model at hand, it is thus also possible to predict and tailor the quantum beats and thus the outgoing photoelectron wave packet. Moreover, the dependence of the quantum beat amplitudes on the ir light intensity can serve as a means to map bound-state dynamics modified by, in our case, the ionizing laser pulse itself to the ionization continuum. There this strong-field-induced dynamics can be analyzed through the quantum beat oscillations in the photoelectron-kinetic-energy distribution. The model is adapted to the situation that the ionization step of the atom can still be treated perturbatively while bound-state couplings induced by one of the applied laser pulses already have to be treated nonperturbatively. The photoelectron-kinetic-energy-resolved quantum beat amplitudes contain information on the population redistribution in the bound states and on Stark shifts of these states while an intense laser pulse is applied to the atom.

Our experimental results also show that in strong-field ionization experiments, which make use of a pump-probe pulse sequence, quantum beat structures in the photoionization continuum, as they were observed, for example, in [4], can significantly be influenced through modifications to the bound-state system of the atom or molecule that is being ionized.

ACKNOWLEDGMENTS

We gratefully acknowledge funding from LASERLAB-EUROPE, Grant Agreement No. 228334, EC's Seventh Framework Program.

[1] A. ten Wolde, L. D. Noordam, A. Lagendijk, and H. B. van Linden van den Heuvell, Phys. Rev. Lett. **61**, 2099 (1988).
[2] S. Zamith, M. A. Bouchene, E. Sokell, C. Nicole, V. Blanchet, and B. Girard, Eur. Phys. J. D **12**, 255 (2000).
[3] S. Gilb, E. A. Torres, and S. R. Leone, J. Phys. B **39**, 4231 (2006).
[4] J. Mauritsson *et al*., Phys. Rev. Lett. **105**, 053001 (2010).
[5] A. Lohr, M. Kleber, R. Kopold, and W. Becker, Phys. Rev. A **55**, R4003 (1997).
[6] A. Becker and F. H. M. Faisal, J. Phys. B **38**, R1 (2005).
[7] R. R. Freeman, P. H. Bucksbaum, H. Milchberg, S. Darack, D. Schumacher, and M. E. Geusic, Phys. Rev. Lett. **59**, 1092 (1987).
[8] P. M. Paul, E. S. Toma, P. Breger, G. Mullot, F. Augé, P. Balcou, H. G. Muller, and P. Agostini, Science **292**, 1689 (2001).
[9] M. A. Baig and J. P. Connerade, J. Phys. B **17**, 1785 (1984).
[10] I. D. Petrov, V. L. Sukhorukov, T. Peters, O. Zehnder, H. J. Wörner, F. Merkt, and H. Hotop, J. Phys. B **39**, 3159 (2006).
[11] R. N. Zare, *Angular Momentum: Understanding Spatial Aspects in Chemistry and Physics. The George Fisher Baker Non-Resident Lectureship in Chemistry at Cornell University*, 1st ed. (Wiley, New York, 1988).
[12] A. F. Starace, J. Phys. B **6**, 76 (1972).
[13] M. J. Seaton, J. Phys. B **31**, 5315 (1998).
[14] K. Harth, J. Ganz, M. Raab, K. T. Lu, J. Geiger, and H. Hotop, J. Phys. B **18**, L825 (1985).
[15] F. Diele, L. Lopez, and R. Peluso, Adv. Comput. Math. **8**, 317 (1998).